

CERIAS Tech Report 2001-26

High Repetition Rate Femtosecond WDM Pulse  
Generation using Direct Space-to-Time Pulse Shapers  
and Arrayed Waveguide Gratings

**D.E. Leaird<sup>1</sup>, S. Shen<sup>1</sup>, A.M. Weiner<sup>1</sup>, A. Sugita<sup>2</sup>  
S. Kamei<sup>2</sup>, M. Ishii<sup>2</sup>, K. Okamoto<sup>2</sup>**  
Center for Education and Research in  
Information Assurance and Security

&

<sup>1</sup>School of Electrical & Computer Engineering,  
Purdue University West Lafayette, IN 47907

<sup>2</sup>NTT Photonics Laboratories

# High Repetition Rate Femtosecond WDM Pulse Generation using Direct Space-to-Time Pulse Shapers and Arrayed Waveguide Gratings

D.E. Leaird<sup>1,2</sup>, A.M. Weiner<sup>1,2</sup>, S. Shen<sup>1</sup>

<sup>1</sup>*School of Electrical & Computer Engineering, Purdue University, West Lafayette, IN 47907-1285, USA  
ph: 765-494-3370, fax: 765-494-6951, leaird@purdue.edu, amw@ecn.purdue.edu, shuai@ecn.purdue.edu*

<sup>2</sup>*Center for Education and Research in Information Assurance and Security – CERIAS  
Purdue University, West Lafayette, IN 47907*

A. Sugita, S. Kamei, M. Ishii, and K. Okamoto

*NTT Photonics Laboratories, 162 Tokai, Naka-gun, Ibaraki-pref., 319-1193, Japan  
sugita@iba.iecl.ntt.co.jp, kamei@iba.iecl.ntt.co.jp, ishii@iba.iecl.ntt.co.jp, okamoto@iba.iecl.ntt.co.jp*

**Abstract:** For the application of high repetition rate WDM pulse train generation from a femtosecond modelocked fiber laser, the direct space-to-time pulse shaper and a properly designed arrayed waveguide grating (AWG) are equivalent. The analogy between the bulk optics and integrated configuration is explored for this application. The critical design parameters of the AWG are the free spectral range and the pathlength difference between adjacent guides in the array.

## I. Introduction

High repetition rate pulse sources are critical components in current and future optical networks. At the highest network data rates in wavelength division multiplexed (WDM) systems, direct modulation of multiple lasers is impractical; so, alternative methods have been explored. For example, tapped delay line structures have been used to generate picosecond pulse trains at rates up to several hundred GHz [1]. Arrayed waveguide grating (AWG) structures, popular for wavelength demultiplexing and routing in WDM communication systems [2] have been used for spectral slicing of supercontinuum [3] and modelocked pulse [4] sources, which results in trains of pulses ~tens of picoseconds in duration at the same repetition rate as the modelocked laser. We have recently demonstrated a completely new scheme utilizing an AWG to generate a high repetition rate burst of short pulses, or in principle a continuous train, at multiple, spatially separated, output wavelengths from a single lower rep rate femtosecond pulse source. Unlike previous work, the pulse repetition rate is determined by the AWG design parameters (not by the modelocked laser) and can be in the range of 500 GHz and greater [5,6].

For our high rate pulse train generation application, the AWG can be shown to be closely analogous to the direct space-to-time (DST) pulse shaper previously demonstrated only in bulk optics [7-12]. Therefore, our previous work on the DST pulse shaper furnishes important insight relevant to this new integrated implementation using an AWG. The main goal of this paper is to discuss and demonstrate this analogy. We first review key results from the bulk optics DST apparatus [9-12]. We then review the integrated (AWG) implementation [5,6], and show that its output can be understood on the basis of the DST pulse shaper analogy. We also present new theoretical results on the relation between the AWG passband and the temporal behavior of the output pulse train.

## II. Direct Space-to-Time Summary

Fig. 1 shown a schematic representation of the bulk optics DST pulse shaper. As the DST components suggest (diffraction grating, lens, and slit) the space-time mapping of the DST can be understood in terms of a generalized spectrometer where a spatially patterned mask is present at the surface of a diffraction grating. The lens collects and focuses the spatially dispersed frequency components of the input beam that are diffracted from the grating. At the Fourier plane of the pulse shaping lens, a thin slit filters the dispersed spectrum, and in the ideal case generates a spatially homogenous output beam whose temporal intensity profile is given by scaled replica of the spatial masking function present at the diffraction grating. We have discussed the operation of this apparatus, including its space-to-time scaling, chirp control properties, multiwavelength potential, and efficiency in detail in earlier publications [9-12]. Here we present a summary of the relevant results.

If the input to the apparatus is an optical pulse of short duration with a spatial profile given by  $s(x)$ , then the field just after diffracting from the grating is given by [13,14]:

$$e_2(x, t) \propto \int d\omega E_2(x, \omega) \exp(j\omega t)$$

where

$$E_2(x, \omega) \propto s(\beta x) \exp(-j\gamma\omega x) E_{in}(\omega) \quad (1)$$

the spatial dispersion,  $\gamma$ , is given by

$$\gamma = \frac{n \lambda}{c} \frac{d\theta_d}{d\lambda} = \frac{m \lambda}{c d \cos \theta_d} \quad (2)$$

where  $\lambda$  is the free space center wavelength,  $n$  is the refractive index of the medium,  $c$  is the speed of light in vacuum,  $d$  is the period of the diffraction grating,  $m$  is the grating diffraction order, and  $\theta_d$  is the angle of diffraction. The astigmatism of the diffracting grating is included with the term  $\beta = \frac{\cos \theta_i}{\cos \theta_d}$ , with the incident angle given by  $\theta_i$ . If the grating-lens, and lens-output slit separations,  $d_1$  and  $d_2$  respectively in Fig. 1, are set equal to the focal length of the lens,  $f$ , then the field just before the output slit is the spatial Fourier transform of eq. (1) [15].

$$E_3(x, \omega) \propto \int dx_2 E_2(x_2, \omega) \exp\left(\frac{j 2\pi n x}{\lambda f} x_2\right)$$

$$e_3(x, t) \propto \int d\omega E_{in}(\omega) S\left(\frac{2\pi n x}{\beta \lambda f} - \frac{\gamma \omega}{\beta}\right) \exp(j\omega t) \quad (3)$$

where  $S(k)$  is the Fourier transform of  $s(x)$ . Assuming an ideal thin slit at the apparatus output, and calling the transverse output slit position  $x = x_s$  yields the spectrum just after the output slit:

$$E_4(x, \omega) \propto S\left(\frac{2\pi n x}{\beta \lambda f} - \frac{\gamma \omega}{\beta}\right) E_{in}(\omega) \delta(x - x_s) \quad (4)$$

Note that  $S(\dots)$  is the spectral response function of the generalized spectrometer. Equation. (4) shows that a transverse movement of the output slit leads to a simple shift in the spectral response function of the DST pulse shaper, just as it would in an ordinary spectrometer, even though the spectral response of the DST may be much more complex than that of a spectrometer.

The time domain response corresponding to eq. (4) is given by

$$e_{out}(t) \propto e_{in}(t) * \left\{ s\left(\frac{-\beta t}{\gamma}\right) \exp\left[\frac{j 2\pi n x_s}{\gamma \lambda f} t\right] \right\} \quad (5)$$

where the "\*" sign denotes convolution. The impulse response function is given by the terms inside the {...} sign and consists of two terms. The first,  $s(-\beta t/\gamma)$ , represents the space-to-time conversion operator –

the output temporal profile consists of a scaled representation of the input spatial profile convolved with the input pulse. The second, linear phase term represents a frequency shift. Thus, a lateral movement of the output slit tunes the output optical frequency while leaving the intensity profile of the shaped output waveform unaffected.

We can also consider a multiple output slit element which spatially separates each output beam in a non-overlapping manner. The output from each independent slit is still given by equations (4) and (5), with the appropriate slit position inserted for  $x_s$ . Thus, the DST pulse shaper should be able to simultaneously generate multiple spatially separated, wavelength shifted outputs, each with the identical intensity profile. Fig. 2 shows intensity cross correlation measurements of output waveforms from the DST apparatus for two different transverse positions of the output slit [10]. The spatial profile at the diffraction grating that is mapped to the time domain as described above is generated by passing the input beam, with its roughly Gaussian spatial profile, through a spatially patterned mask consisting of transparent and opaque regions. The left column of Fig. 2 corresponds to a periodic masking function while the right column corresponds to a modulated 'data packet' where some of the transparent features of the periodic mask are blocked. The spatial profile after passing through the patterned mask is then imaged onto the diffraction grating. The total space-to-time conversion constant, from the spatially patterned mask to the apparatus output, consists of the term presented earlier,  $\gamma/\beta$ , multiplied by the imaging system magnification. The roll-off in the output temporal intensity profile in Fig. 2 is due to the Gaussian spatial profile of the input beam. The form of the output temporal profile, a periodic burst of twenty pulses, is identical as the pulse shaping slit is moved transversely across the output plane, as expected from eq. (5).

Our DST pulse shaper experiments, as described above, relied on a modelocked Ti:S laser producing  $\sim 100$  fs pulses at an 850 nm center wavelength as the source. The pulse shaping apparatus employed an 1800 line/mm grating, a diffraction angle,  $\theta_d \approx 54^\circ$ , and a 160 mm focal length lens.

Fig. 3 shows power spectra recorded of the output of the DST pulse shaper, using the same periodic spatially patterned mask as was used in the left column of Fig. 2, for a series of different transverse output slit positions [10]. The periodic multiply peaked nature of the power spectra is expected from the periodic multiply peaked nature of the intensity cross correlation measurements shown in Fig. 2. As the

pulse shaping slit is translated transversely across the output plane, the shape of the recorded power spectra remains invariant while the center wavelength shifts.

We also discuss the case where the distance between the diffraction grating and pulse shaping lens,  $d_1$ , and the pulse shaping lens and slit,  $d_2$ , are permitted to vary away from the focal length of the pulse shaping lens,  $f$  [12]. We assume the input spatial profile  $s(x)$  is given by a spatial masking pattern,  $m(x)$ , multiplied by a Gaussian beam profile of radius  $w$ , i.e.,

$$s(x) = m(x) \exp\left[\frac{-x^2}{w^2}\right] \quad (6)$$

The output field, for a transverse output slit position  $x_s = 0$ , is written [12]:

$$e_{\text{out}}(t) \propto e_{\text{in}}(t) * \{N(t) \exp[-j\phi(t)]\} \quad (7)$$

where

$$N(t) = m\left(\frac{-\beta t}{\gamma}\right) \exp\left[\frac{-\beta^2 t^2}{\gamma^2 w^2}\right] \quad (8)$$

determines the temporal intensity profile and

$$\phi(t) = \frac{\pi}{\lambda \gamma^2} \left( \frac{\beta^2}{R} - \frac{d_2 - f}{d_1 f + d_2 f - d_1 d_2} \right) t^2 \quad (9)$$

gives the quadratic temporal phase and hence the chirp.  $R$  is the phase front radius of curvature of the spatial profile at the diffraction grating. When  $d_1 = d_2 = f$ , a spatial phase curvature at the grating is mapped into a quadratic temporal phase function. For finite  $R$ , output chirp can be set to zero by adjusting  $d_1$  and  $d_2$  to achieve  $\phi(t) = 0$  (assuming unchirped input pulses). It is interesting to note that in the case of a converging or diverging input beam at the grating (i.e.,  $R \neq \infty$ ), the beam is brought to a focus at a position other than the back focal plane of the lens. By using ABCD matrices, one can easily show that for  $d_1$  and  $d_2$  yielding  $\phi(t) = 0$ , an input Gaussian beam with phase front radius of curvature  $R$  is brought to focus at exactly the position of the pulse shaping slit. The intensity profile and space-to-time conversion constant are expected to remain invariant as the chirp is manipulated in this way.

Unlike the well known grating and lens pulse stretcher [13], the chirp in the DST pulse shaper is most strongly affected by the lens-slit separation ( $d_2$ ). When  $d_2$  is fixed at the focal length of the lens ( $d_2 = f$ ), output chirp is independent of the diffraction grating – lens separation,  $d_1$ . When both  $d_1$  and  $d_2$  are set equal to the focal length of the pulse shaping lens, the output temporal field shown in eq. (7) simplifies to

$$e_{\text{out}}(t) \simeq \exp\left[\frac{-\beta^2 t^2}{\gamma^2 w^2}\right] \exp\left[\frac{-j k \beta^2 t^2}{2 R \gamma^2}\right] \quad (10)$$

The above expression assumes that the input beam is a simple unpatterned Gaussian beam. In this special case it is evident that the only chirp on the output waveform due to the DST pulse shaping apparatus arises from the spatial phase front radius of curvature of the beam at the diffraction grating. In this case, assuming a bandwidth limited input pulse, a measurement of the chirp out of the DST pulse shaper gives a measure of the phase front curvature present at the diffraction grating. After measuring the phase front curvature in this way, the chirp can be predicted for any other combination of the grating-lens ( $d_1$ ) and lens-slit ( $d_2$ ) separations.

Fig. 4 shows the measured chirp in two special cases of eq. (7)-(9) [11]. In one case, the diffraction grating-pulse shaping lens separation,  $d_1$ , is allowed to vary while the pulse shaping lens – output slit separation,  $d_2$ , is fixed at the focal length of the lens,  $f$ . In the second case the converse is true,  $d_2$  is varied while  $d_1 = f$  is maintained. In the first case, the output chirp does not change with  $d_1$  as expected from our prediction.

Two specific implementations of the general case of eq. (7)-(9) (neither  $d_1$  nor  $d_2$  equal to  $f$ ) are shown in Fig. 5, along with the special case of  $d_1 = f$ . In the top trace, the grating-lens separation is set to a fixed value of 110 mm (compared to  $f = 160$  mm), and the predicted chirp is plotted as a function of the lens-slit separation,  $d_2$ . In the bottom case, both  $d_1$  and  $d_2$  are varied, but their sum is held fixed at twice the focal length of the lens. Both of these new cases are tested by a chirp measurement at  $d_2 = 60$  mm. In each case the calculated and measured chirp are in excellent agreement.

Finally, in order to verify that the output intensity profile is invariant as the chirp is adjusted, intensity cross correlation traces of an ultrafast data packet were recorded for three different amounts of output chirp. The results are shown in Fig. 6 [11], and in all cases  $d_1 = f$ . The top trace was taken in a

moderately chirped configuration when  $d_2 = f$ . The middle trace was taken in a partially compensated chirp configuration,  $d_2 - f = 66$  mm, and the bottom trace was taken in a chirp-free configuration,  $d_2 - f = 119$  mm. The general shape of each of the three cross correlation traces is the same verifying that the output intensity profile is unchanged as the chirp on the DST output is varied. The minor differences in the envelopes of the three traces is due to slight changes in the centering of the pixelation mask on the input beam from one measurement to the next.

### III. Pulsed AWG: theory

#### A. Analogy between the AWG and the DST pulse shaper

A standard integrated AWG structure is shown in Fig. 7 [2,16]. From the perspective of the DST pulse shaper of Fig. 1, we view the waveguide array as equivalent to a curved diffraction grating. This is analogous to the grating/lens combination of the DST with  $d_1 = 0$ . The output waveguides of the AWG are analogous to a multiple element output slit in the DST pulse shaper. The waveguide array – output slit separation is equal to the focal length for light emerging from the waveguide array; therefore  $d_2 = f$ . The spatially modulated field pattern at the output of the waveguide array section is equivalent to a periodically modulated spatial pattern in the DST. By analogy, under appropriate conditions, an AWG read out by a femtosecond pulse should lead to a very high repetition rate femtosecond pulse train. The combination of the grating and lens into a single element does not modify the character of the output since we know from the work in the DST pulse shaper that the combination  $d_1 = 0$ ,  $d_2 = f$  does not introduce any chirp. Of course, no chirp on the output of the AWG device is only strictly true assuming that the waveguide dispersion is negligible within the AWG device itself.

For short pulse applications, the important AWG parameter determining the character of the output is the free spectral range (FSR), which is equal to the inverse of the delay increment per guide ( $\Delta\tau$ ):

$$\text{FSR} = \Delta\tau^{-1} = \frac{c}{n_{\text{eff}} \Delta L} \quad (11)$$

where  $n_{\text{eff}}$  is the effective index of the waveguide,  $c$  is the speed of light in vacuum, and  $\Delta L$  is the physical path length difference from one guide to the next in the waveguide array section of the AWG. The key design constraint of the AWG is that the free spectral range (FSR) must be less than the optical bandwidth,

$\Delta\nu$ , of the source laser. In this case, the output spectrum of any single waveguide in the AWG is multiply peaked, with the spectral peak spacing equal to the FSR. Conversely, this means that the bandwidth limited input pulse width,  $t_p$ , is less than the delay increment per guide,  $\Delta\tau$ , in the waveguide array. The time domain output then consists of a train of pulses with pulse separation,  $\Delta\tau$ , equal to the waveguide array delay increment. The duration of the individual output pulses is the same as the input pulse, and the duration of the envelope of the pulse train varies inversely with the AWG passband width. We note that the requirement that  $\text{FSR} < \Delta\nu$  is opposite to the normal usage in DWDM systems, where the free spectral range must exceed the range of wavelengths employed.

Alternatively, the pulse-to-pulse separation in the output pulse train burst can be calculated by viewing the AWG as an integrated version of a DST pulse shaper. Viewed this way, the pulse repetition period  $\Delta T$  is given by:

$$\Delta T = a \left( \frac{\gamma}{\beta} \right)_{\text{AWG}} \quad (12)$$

where  $a$  is the pitch of the waveguide array at the interface of the waveguide array and output slab waveguide and  $(\gamma/\beta)_{\text{AWG}}$  is the space to time conversion constant for the arrayed waveguide grating.  $\gamma$  in eq. (12) is calculated according to eq. (2) with  $n = n_s$ , the effective slab waveguide refractive index, and where  $\frac{d\theta_d}{d\lambda}$  is expressed for the AWG as [17]:

$$\frac{d\theta_d}{d\lambda} = \frac{m n_g}{a n_s n_c} \quad (13)$$

The grating order,  $m$ , is given by

$$m = \frac{n_c \Delta L}{\lambda} \quad (14)$$

$n_c$  is the effective index of the waveguide array, and  $n_g$  is the group index of the waveguide array, and  $\lambda$  is defined as the free space wavelength. The astigmatism parameter  $\beta$  is assumed to be 1, or  $\theta_d \approx \theta_i \approx 0$  which is a reasonable assumption given typical dimensions of AWG devices. Therefore,

$$\left(\frac{\gamma}{\beta}\right)_{\text{AWG}} \approx \gamma_{\text{AWG}} = \frac{n_s \lambda}{c} \frac{n_c \Delta L}{\lambda} \frac{n_g}{a n_s n_c} = \frac{\Delta L n_g}{a c} \quad (15)$$

From eq. (12), the pulse repetition period is given by

$$\Delta T = \frac{\Delta L n_g}{c} \quad (16)$$

This is exactly equal to the delay increment per waveguide,  $\Delta\tau$ , which is the expected pulse separation based on the earlier argument. This supports our view of the response of the AWG as analogous to that of the DST pulse shaper.

### B. Temporal window of the pulsed AWG

In the DST pulse shaper/AWG analogy, the AWG output waveguide takes the role of the DST output slit. The actual output field for the pulsed AWG is given by performing the overlap integral between the field just before the waveguide and the waveguide mode. Using eq. (3), the field in the output guide,  $e_G(x,t)$ , can be written

$$e_G(x,t) \propto a\left(\frac{x}{x_0}\right) \int d\omega \exp(j\omega t) E_{\text{in}}(\omega) \int dx' a\left(\frac{x'}{x_0}\right) S\left[\left(\frac{-\gamma}{\beta}\right) \left(\omega - \frac{k x'}{\gamma f}\right)\right] \quad (17)$$

Here  $k = \frac{2\pi n}{\lambda}$ ,  $S(q)$  is the Fourier transform of the spatial profile at the output of the waveguide array

section  $s(x)$ , and  $a\left(\frac{x}{x_0}\right)$  is the electric field spatial profile of the guided mode. The  $x_0$  parameter allows

the size of the waveguide mode to be varied. We have assumed here that output guide is centered at  $x = 0$ ,

and that  $a\left(\frac{x}{x_0}\right)$  is normalized such that

$$\int dx \left| a\left(\frac{x}{x_0}\right) \right|^2 = 1 \quad (18)$$

Note that the single mode output guide enforces that all the frequencies have the same spatial profile at the output.

We can gain insight into the temporal behavior of the output by manipulating eq. (17):

$$\begin{aligned} e_G(x,t) &\propto a\left(\frac{x}{x_0}\right) \int dx' a\left(\frac{x'}{x_0}\right) \int d\omega \exp(j\omega t) E_{in}(\omega) S\left[\left(\frac{-\gamma}{\beta}\right) \left(\omega - \frac{k x'}{\gamma f}\right)\right] \\ &\propto a\left(\frac{x}{x_0}\right) \int dx' a\left(\frac{x'}{x_0}\right) e_{in}(t) * \left\{ s\left(\frac{-\beta t}{\gamma}\right) \exp\left[\frac{j k x' t}{\gamma f}\right] \right\} \end{aligned} \quad (19)$$

Changing the order of the integrals again, we obtain

$$\begin{aligned} e_G(x,t) &\propto a\left(\frac{x}{x_0}\right) e_{in}(t) * \left\{ s\left(\frac{-\beta t}{\gamma}\right) \int dx' a\left(\frac{x'}{x_0}\right) \exp\left[\frac{j k x' t}{\gamma f}\right] \right\} \\ &\propto a\left(\frac{x}{x_0}\right) e_{in}(t) * \left\{ s\left(\frac{-\beta t}{\gamma}\right) A\left(\frac{-k x_0 t}{\gamma f}\right) \right\} \end{aligned} \quad (20)$$

Where

$$A(q) = \int du a(u) \exp(-jqu) \quad (21)$$

is the spatial Fourier transform of the mode profile function. Equation (20) shows that the impulse response function of the pulsed AWG is given by the product of appropriately scaled versions of the spatial profile and the Fourier transform of the mode profile function. The finite size of the waveguide mode leads to a temporal window function which restricts the temporal range of output waveforms generated by the pulsed AWG. The width of the temporal window is inversely proportional to the size of the waveguide mode ( $x_0$ ).

If we rewrite eq. (20) in terms of the frequency domain variables, we obtain

$$e_G(x,t) \propto a\left(\frac{x}{x_0}\right) \int d\omega \exp(j\omega t) E_{in}(\omega) \left[ S\left(\frac{-\gamma\omega}{\beta}\right) * a\left(\frac{-\gamma f \omega}{k x_0}\right) \right] \quad (22)$$

The expression inside the brackets is simply the normal frequency response of the AWG (in terms of the spatial amplitude). Therefore, we have the result that the pulse shaping function in the time domain (including the effect of the window function) is exactly the inverse Fourier transform of the AWG frequency response.

Several points are worth discussion:

- (1) The analysis is easily extended to output waveguides centered at positions  $x_s \neq 0$ . The only difference is the introduction of a frequency shift, exactly as in eq. (5).
- (2) Very similar results were previously derived for the bulk optics DST pulse shaper using an output slit rather than a waveguide [12]. In particular, the temporal window function and the spectral response function are still governed via a Fourier transform relationship, and the temporal window width varies inversely with the width of the slit.
- (3) The origin of the temporal window for the pulsed AWG can be understood simply in terms of the finite acceptance angle of the output waveguide. Larger delays correspond to propagation in guides in the waveguide array section further from the center guide, and hence are incident on the output guide at larger angles. A temporal window results since the larger angles are coupled less effectively into the output guide.

### C. Efficiency of the pulsed AWG

The efficiency of the pulsed AWG, defined as the ratio of the output power from a particular guide to the input power to the AWG, is given ideally by

$$\eta = \frac{\int d\omega \left| E_{in}(\omega) \int dx a\left(\frac{x}{x_0}\right) S\left[\left(\frac{-\gamma}{\beta}\right) \left(\omega - \frac{kx}{\gamma f}\right)\right] \right|^2}{\iint d\omega dx |E_{in}(\omega)|^2 \left| S\left[\left(\frac{-\gamma}{\beta}\right) \left(\omega - \frac{kx}{\gamma f}\right)\right] \right|^2} \quad (23)$$

A similar (not identical) expression for the efficiency of a DST pulse shaper was reported in [12]. Following the more detailed discussion in [12], we note that pulse train generation from an AWG inherently entails loss, due to the spectral filtering operation involved. In general, the efficiency decreases as the width of the output temporal window increases. Similar to the DST pulse shaper, much of the missing power appears in the form of identical but wavelength shifted pulse trains emerging from the other output waveguides.

## IV. Pulsed AWG: experiments

In the AWG experiments described here, a modelocked erbium fiber laser producing a 50 MHz train of  $\sim 200$  fs pulses at 1560 nm is utilized. In principle, similar experiments can also be performed using much higher rate (e.g.  $>10$  GHz) modelocked pulse sources. Two different AWG devices were used, each with a 1 THz FSR corresponding to a 1 ps delay increment per guide in the waveguide array. One device has 100 GHz output channel spacing (0.41 nm 3dB passband width) and 40 channels while the other device has 40 GHz output channel spacing (0.17 nm 3dB passband width) and 100 channels; although, not all channels were fiber coupled. The experimental results have also been described in [5,6].

Fig. 8 shows power spectra recorded from an AWG device with 40 GHz output channel spacing. The power spectrum of the source laser is overlaid with the output power spectra recorded from channels 1 and 4. The 1 THz FSR is evident from the periodic passband structure with 8.1 nm spacing between peaks. The spectra consist of six discrete output frequencies within the bandwidth of the source laser for each output channel. The shift in output center wavelength from one output to another is apparent as well. The multiply peaked nature of the power spectra demonstrate that  $\Delta\nu > \text{FSR}$ ; therefore, the output temporal profile is expected to be a train of pulses where the temporal period of the pulses in the output train is given by the inverse of the FSR.

Fig. 9 shows intensity cross correlation measurements of two different AWG devices – the 40 GHz output channel spacing device used in the power spectra measurements of Fig. 8, and a 100 GHz output channel spacing device. As expected from the power spectrum presented above the temporal profile consists of a train of pulses with a 1 ps period, corresponding to the AWG delay increment, which is the inverse of the FSR, and with a pulse duration comparable to that of the input pulse. The temporal window (or number of pulses) is inversely proportional to the AWG filter bandwidth and therefore increases by 2.5 times from the 100 GHz device to the 40 GHz device. The form of the output intensity profile is the same for different output channels of a single device, even though the spectrum is shifted, which is identical to the multiple wavelength nature of the bulk optics DST presented above. In Fig. 9C, the calculated pulse envelope is shown for the 100 GHz output channel spacing device (dashed line) overlaid with the measured temporal intensity profile (solid line). The envelope is calculated from a measurement of a single passband

in the power spectrum. If we denote the form of the passband as  $|A(\omega)|^2$ , the envelope,  $|a(t)|^2$ , is taken as

$$|a(t)|^2 = \left| \frac{1}{2\pi} \int d\omega \sqrt{|A(\omega)|^2} \exp(j\omega t) \right|^2 \quad (24)$$

The actual envelope is in excellent agreement with this calculation confirming the inverse relationship between the AWG passband function and the envelope of the output pulse sequence, as predicted in the previous section.

## V. Conclusion

In summary, the femtosecond response of an arrayed waveguide grating designed to have a free spectral range less than the bandwidth of the input pulse has been shown to be analogous to that of a bulk optics direct space-to-time pulse shaper. Under such conditions the AWG produces a very high repetition rate output pulse sequence with the output pulse period determined by the physical path length difference between adjacent guides in the waveguide array. Both the bulk optics DST pulse shaper and the integrated AWG are capable of generating multiple spatially separated output channels with identical temporal intensity profiles but shifted in center wavelength. This ability to generate very high repetition rate (100s of GHz to  $\geq 1$  THz) pulse trains, including multiple wavelength shifted versions of such pulse trains, may find application in ultrahigh speed TDM and hybrid WDM-TDM optical communications and networking.

## Acknowledgment

This material is based upon work supported by, or in part by the U.S. Army Research Office under contract DAAG55-98-1-0514, and by sponsors of the Center for Education and Research in Information Assurance and Security. Also, we thank IMRA America for the loan of the femtosecond modelocked fiber laser used in the AWG experiments.

## References

1. S. Kawanishi, "Ultrahigh-speed optical time-division-multiplexed transmission technology based on optical signal processing," *IEEE J. Quant. Electron.*, **34**, 2064-2079 (1998).
2. K. Okamoto, "Recent progress of integrated optics planar lightwave circuits," *Opt. and Quant. Electron.*, **31**, 107-129 (1999).
3. S. Kawanishi, H. Takara, K. Uchiyama, I. Shake, and K. Mori, "3 Tbit/s (106 Gbit/s x 19 channel) optical TDM and WDM transmission experiment," *Electron. Lett.* **35**, 826-827 (1999).

4. I.Y. Khrushchev, J.D. Bainbridge, J.E.A. Whiteaway, I.H. White, and R.V. Penty, "Multiwavelength pulse source for OTDM/WDM applications based on arrayed waveguide grating," *IEEE Photon. Tech. Lett.*, **11**, 1659-1661 (1999)
5. D.E. Leaird, S. Shen, A.M. Weiner, A. Sugita, S. Kamei, M. Ishii, and K. Okamoto, "1 THz Repetition Rate WDM Pulse Train Generation from an Arrayed-Waveguide Grating," in *Conference on Lasers and Electro-Optics Postdeadline Papers*, CPD18 (2000).
6. D.E. Leaird, S. Shen, A.M. Weiner, A. Sugita, S. Kamei, M. Ishii, and K. Okamoto, "Generation of High Repetition Rate WDM Pulse Trains from an Arrayed-Waveguide Grating," submitted to *IEEE Photon. Tech. Lett.*
7. B. Colombeau, M. Vampouille, and C. Froehly, "Shaping of Short Laser Pulses by Passive Optical Fourier Techniques," *Opt. Comm.*, **19**, 201-204 (1976).
8. C. Froehly, B. Colombeau, and M. Vampouille, "Shaping and analysis of picosecond light pulses" in *Progress in Optics*, E. Wolf, Ed. **20**, 65 (1983).
9. D.E. Leaird, and A.M. Weiner, "Femtosecond optical packet generation by a direct space-to-time pulse shaper," *Opt. Lett.* **24**, 853-855 (1999).
10. D.E. Leaird, and A.M. Weiner, "Wavelength tunable femtosecond pulse trains from a direct space-to-time pulse shaper," in *Conference on Lasers and Electro-Optics*, OSA Technical Digest, 410-411 (2000).
11. D.E. Leaird, and A.M. Weiner, "Chirp control in the direct space-to-time pulse shaper," *Opt. Lett.* , 850-852 (2000).
12. D.E. Leaird, and A.M. Weiner, "Femtosecond Direct Space-to-Time Pulse Shaping," submitted to *IEEE J. Quant. Electron.*
13. O. Martinez, "Grating and prism compressors in the case of finite beam size," *J. Opt. Soc. Am. B*, **3**, 929-934, (1986).
14. M. Wefers, and K.A. Nelson, "Space-time profiles of shaped ultrafast optical waveforms," *IEEE J. Quant. Electron.*, **32**, 161-172, (1996).
15. J.W. Goodman, *Introduction to Fourier Optics* (McGraw-Hill, New York, 1968).
16. R. Adar, C.H. Henry, C. Dragone, R.C. Kistler, M.A. Milbrodt, "Broad-band array multiplexers made with silica wave-guides on silicon," *J. Lightwave Tech.*, **11**, 212-219, (1993).
17. H. Takahashi, K. Oda, H. Toba, and Y. Inoue, "Transmission characteristics of arrayed waveguide NxN wavelength multiplexer," *Journ. Light. Tech.*, **13**, 447-455 (1995).

## Figure Captions

Fig. 1 Schematic diagram of the bulk optics DST pulse shaper.

Fig. 2 Intensity cross correlation measurements of the DST pulse shaper output for a periodic pixelation mask (left), and a 'data packet' mask (right). Top and Bottom traces recorded for transverse pulse shaping slit positions separated by 2 mm.

Fig. 3 Power spectra of the DST pulse shaper output as a function of transverse pulse shaping slit position with a periodic pixelation mask.

Fig. 4 Measured and calculated chirp for two special cases of grating-lens, and lens-slit separation. Solid line is calculated for grating-lens separation held at the focal length of the pulse shaping lens, but lens-slit allowed to vary. Triangles are measured data for the  $d_1 = f$  configuration. Dash-dot line is calculated for lens-slit separation held at  $f$ , but grating-lens is allowed to vary. Squares are measured data for the  $d_2 = f$  configuration.

Fig. 5 Calculated and measured chirp as a function of lens-slit separation. Lines are calculated values while symbols are measured.

Fig. 6 Intensity cross correlation measurements of the DST output for three different values of output chirp. A 'data packet' pixelation mask is employed. A) is a heavily chirped configuration, B) is moderately chirped, and C) is near zero chirp.

Fig. 7 Arrayed waveguide grating device.

Fig. 8 Power spectra recorded from the output of the 40 GHz output channel spacing AWG on a semi-log scale.

Fig. 9 Output pulse trains from the AWG. A) and C) Measured intensity cross correlation from the 100 GHz output channel spacing (solid lines). Dashed line in C) is the calculated temporal window. B) and D) are measured temporal profiles from two different output channels of the 40 GHz output channel spacing AWG.

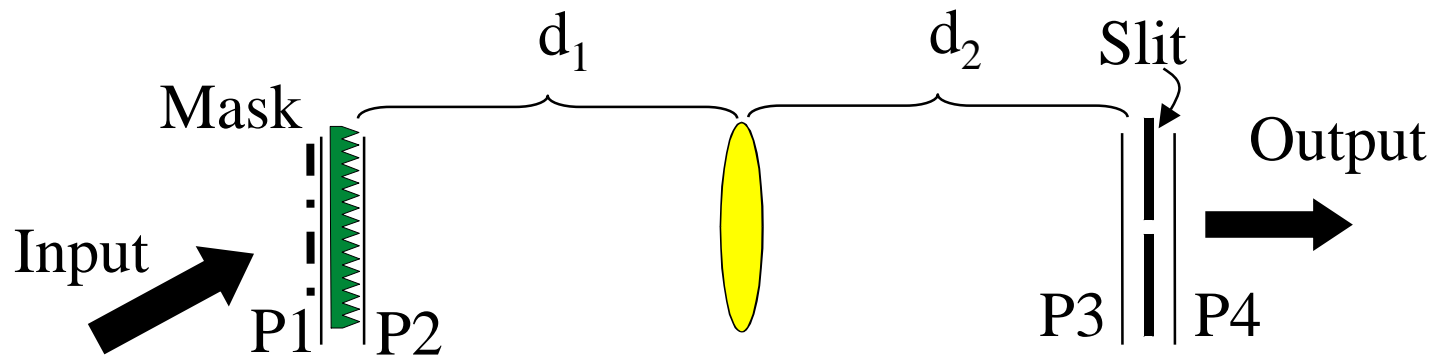


Figure 1

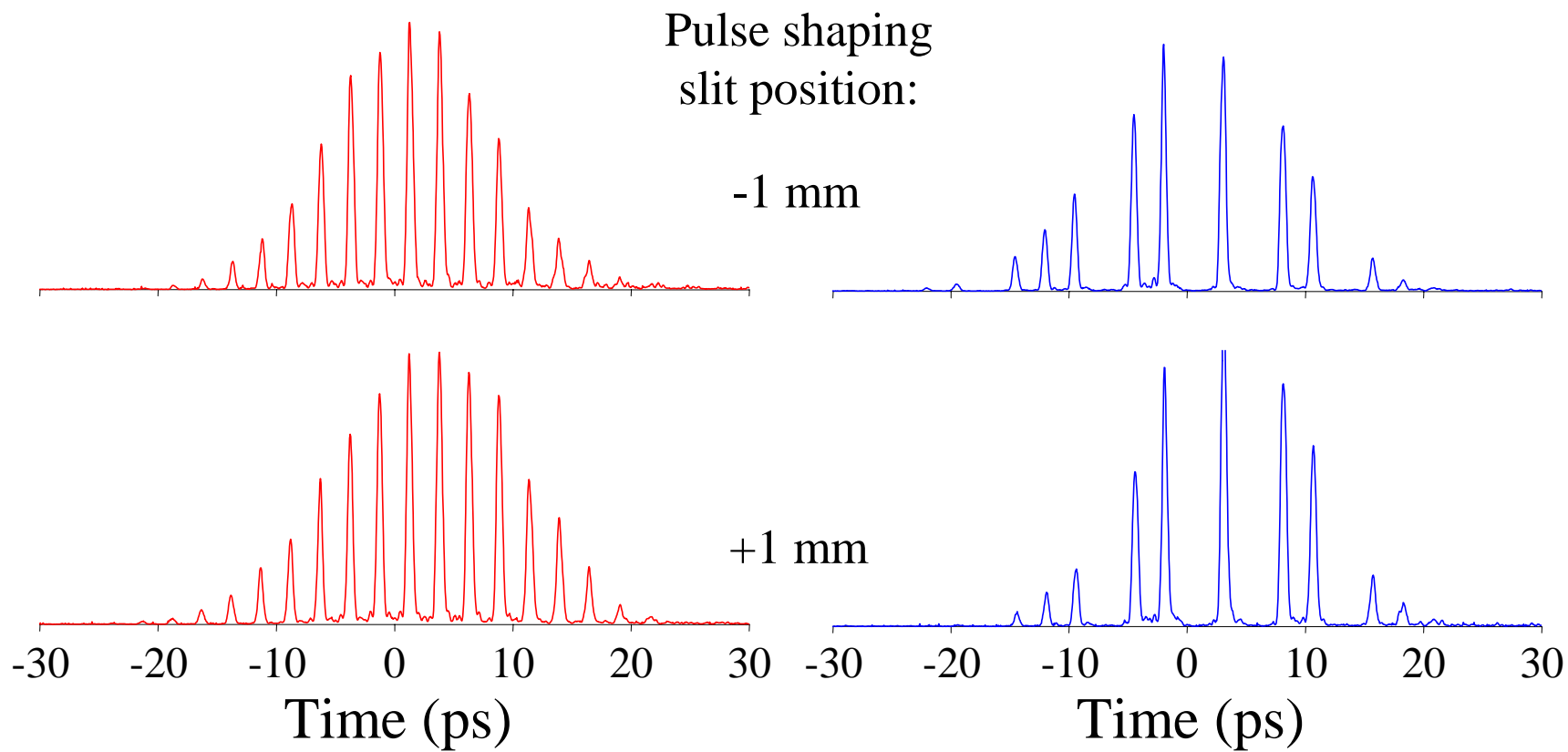


Figure 2

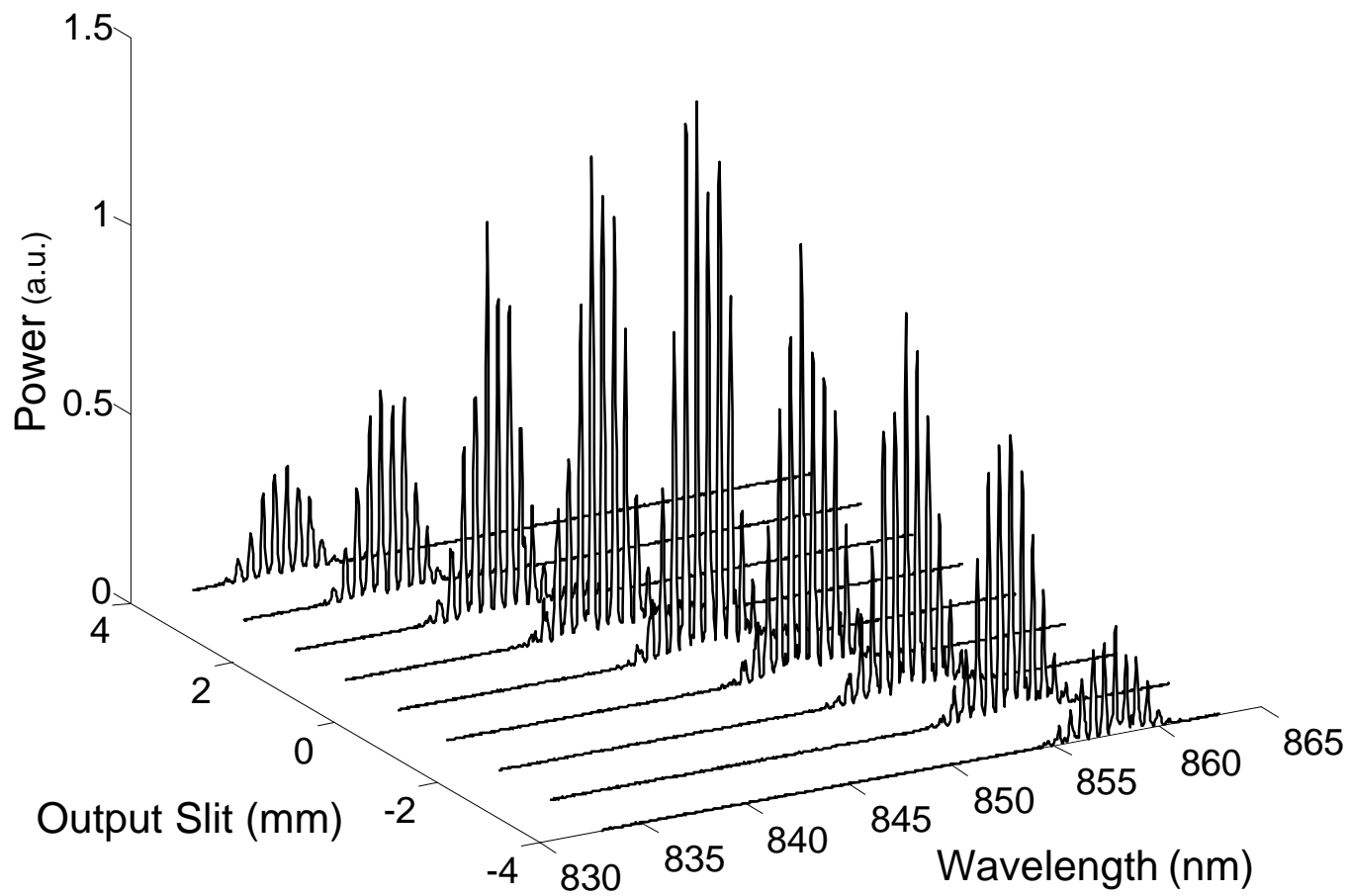


Figure 3

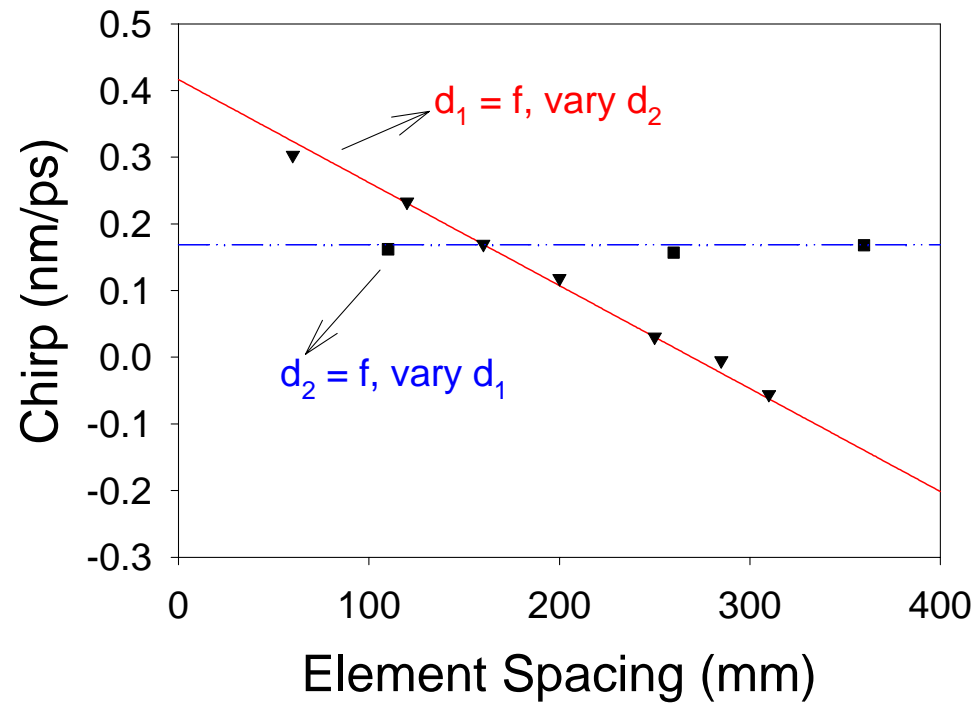


Figure 4

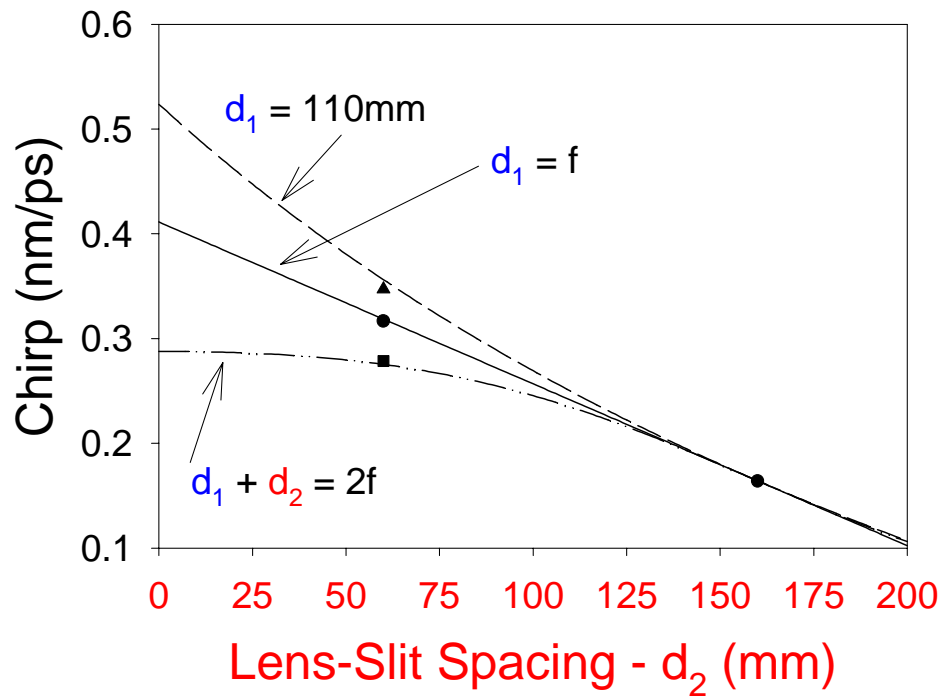


Figure 5

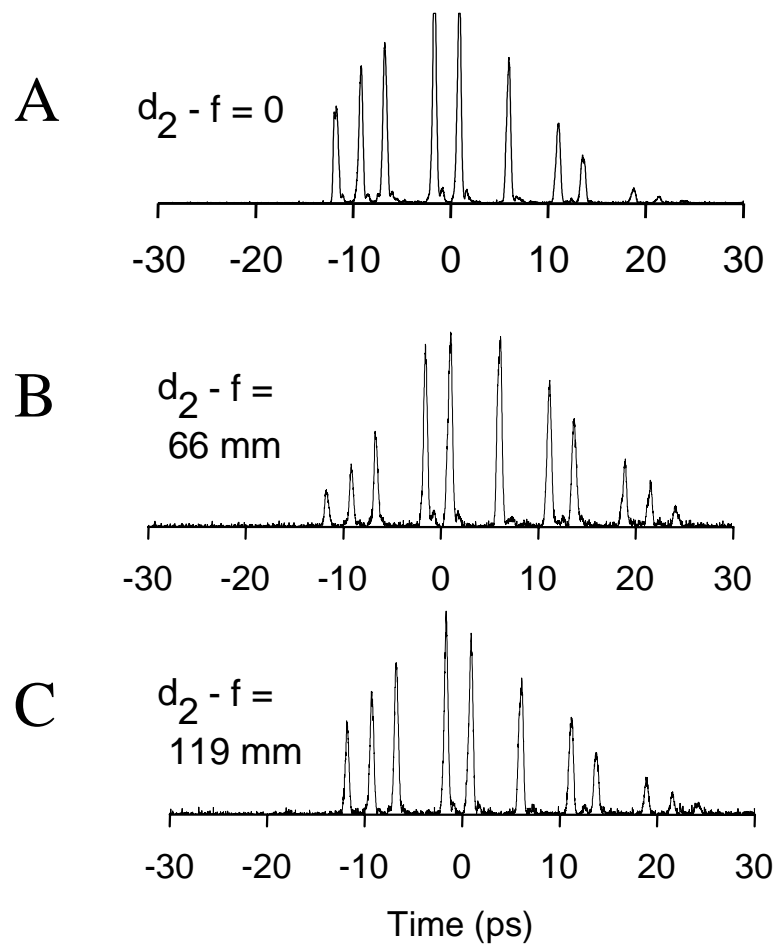


Figure 6

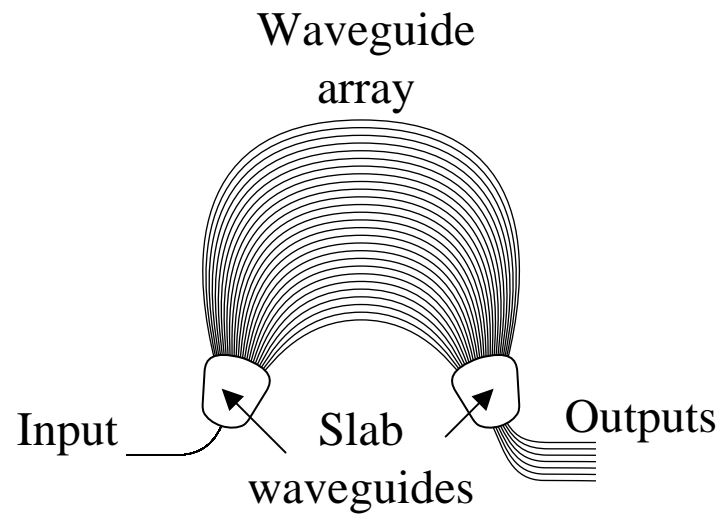


Figure 7

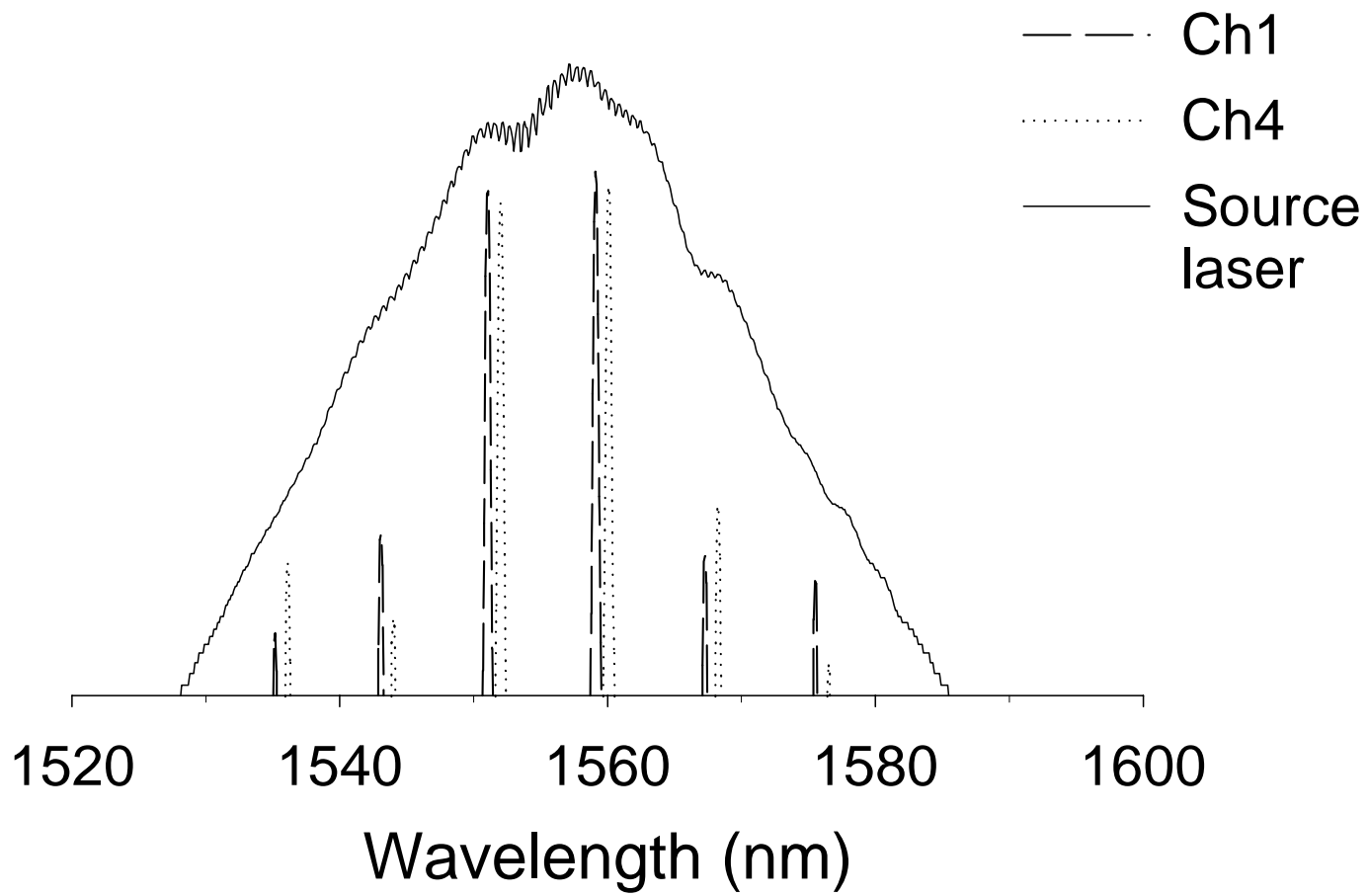


Figure 8

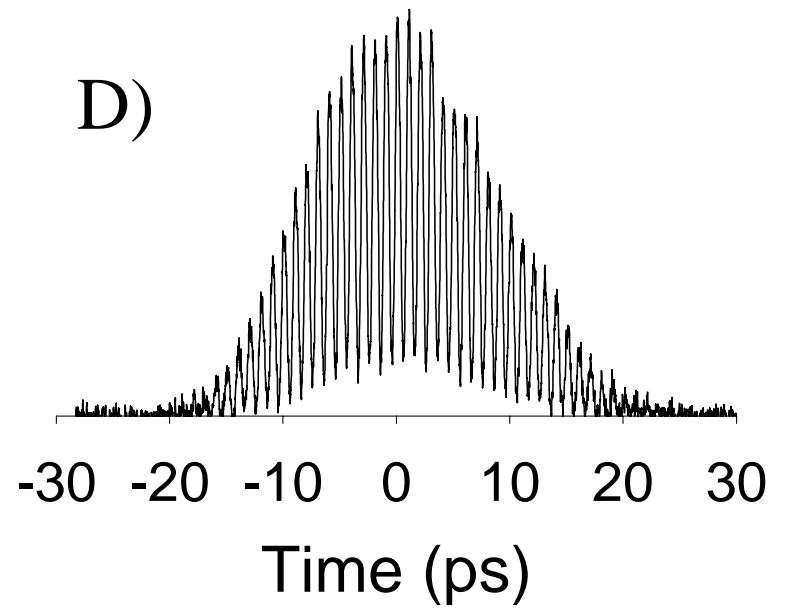
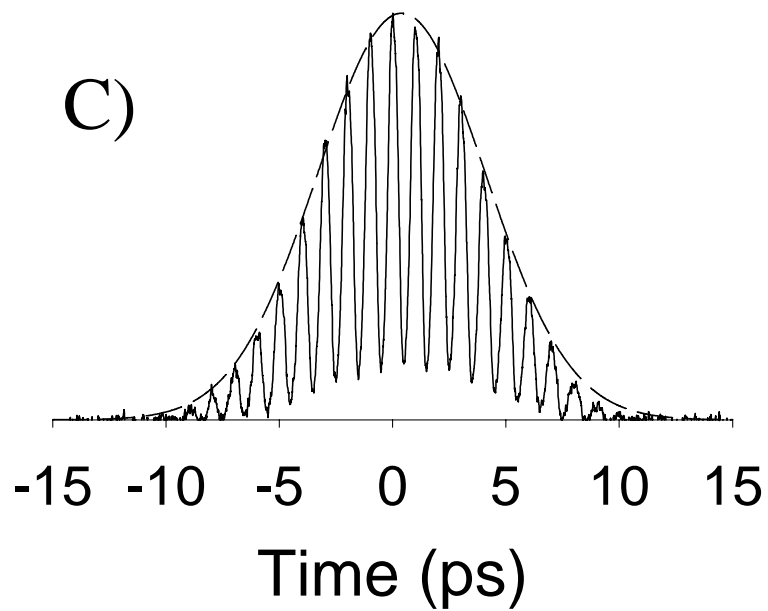
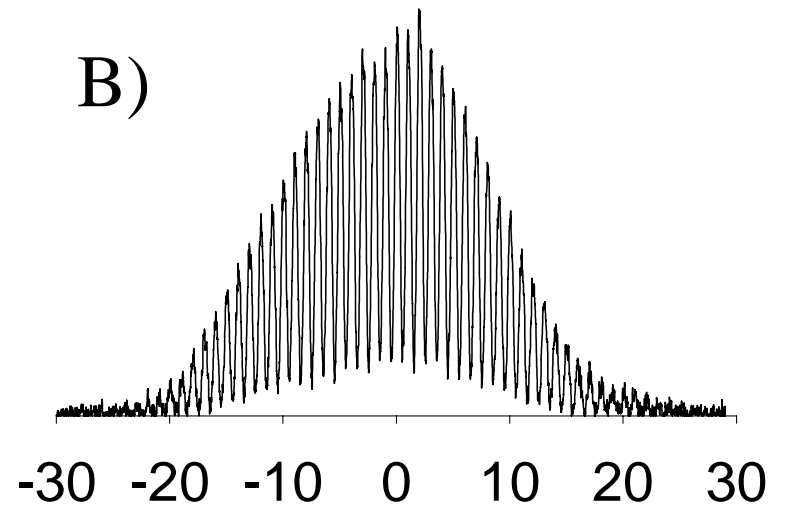
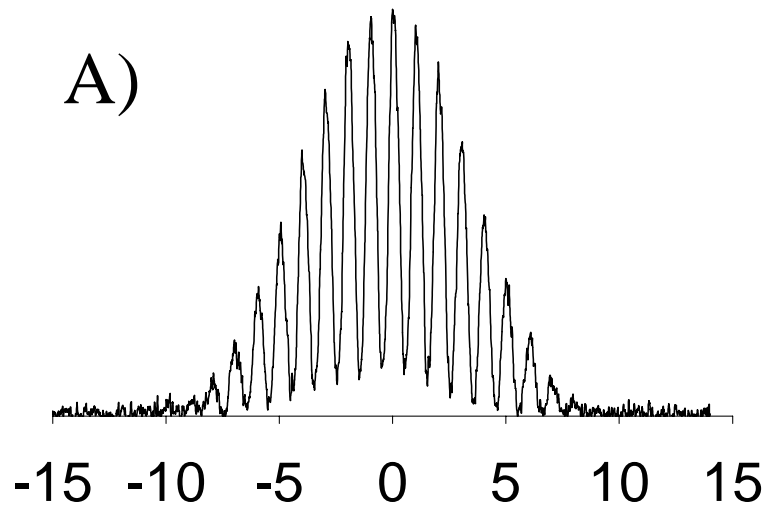


Figure 9